Concluding Remarks and Future Directions

This thesis centers on the redox cycling of manganese and how the redox state of manganese can reveal environmental conditions and biological processes. Chapter 1 presents the current knowledge of manganese oxidation and reduction reactions and analyses of a series of representative manganese-enriched sedimentary rocks ('manganese deposits') throughout geologic time. This mineralogical survey of manganese deposits concluded that manganese is generally stabilized in the geologic record in a different and more reduced form (like in Mn(II) carbonates or Mn(III) oxides) than the primary precipitate (which is usually Mn(IV) oxides).

Chapter 2 focuses on the origin of the earliest significant manganese deposit, from the 2.415 billion-year-old Koegas Subgroup in South Africa. Here we investigated whether this deposit, which appeared to occur prior to the oxygenation of Earth's atmosphere and ocean, could be evidence for a biological hypothesis that predicted manganese-oxidizing photosynthesis was a precursor to water-oxidizing photosynthesis. Two proxies for oxygen in two cores through the Koegas Subgroup indicated very low levels of oxygen, but a micro-scale study of the manganese deposits showed these were originally manganese oxides – now stabilized as manganese-enriched carbonates. Finding manganese oxidation before oxygen production strongly supports the presence of manganese-oxidizing photosynthesis, and this study marks the first strong geologic evidence for an evolutionary hypothesis.

As a follow-up report, Chapter 3 probes deeper into one of the proxies for oxygen used in Chapter 2: the oxygen-sensitive detrital grains. In this study, we presented a second redox-sensitive detrital grain, uraninite, in addition to expanding on the abundant detrital pyrite described earlier. We also developed a mathematical model combining physical erosion and chemical weathering processes to constrain ancient oxygen concentrations. For the Koegas Subgroup, the model limits the atmosphere to less than ~ 10^{-5} atm of O_2—not enough to support Mn oxidation as we understand it today.

Chapter 4 returns to manganese cycling, exploring how such a wide variety of manganese deposits become reduced post-deposition using real-time measurements of common manganese reduction pathways. We used a flow-through system to measure redox state and coordination environment of manganese throughout abiotic reduction by sulfide and ferrous iron and biologically-mediated reduction using a model metal-reducing bacteria, *Shewanella oneidensis*, in several end-member conditions. We found that the most common manganese phase in the geologic record, Mn(II)-carbonates, was produced by microbially-mediated manganese oxide reduction, while abiotic reduction pathways (without inorganic carbon present) made Mn(II) in solution. Mn(III) oxyhydroxides were produced as an intermediate in almost all reaction pathways, and these could serve as precursors to the Mn(III) oxides found in ancient manganese deposits.

Chapter 5 is a final investigation into ancient manganese deposits, but this time focusing on the minor Mn deposits reported from prior to the Koegas Subgroup. Manganese oxidation (and therefore O_2) has long since been inferred from manganese enrichment of sedimentary rocks, but another possibility exists: manganese could be enriched from magmatic or hydrothermal fluids associated with alteration occurring at high temperatures and pressures (i.e., during metamorphism). We tested whether metamorphism could mobilize and enrich manganese in ancient rocks harnessing well-understood metamorphic gradients across South Africa. We performed micro-scale and nano-scale analyses of 2.5 billion-year-old correlated strata from the highly metamorphosed eastern basin and the unperturbed western basin and determined that manganese was mobilized during metamorphism and enriched in garnets, amphiboles, and carbonates from metamorphosed samples, and occasionally enriched in bulk concentrations. These results are limited to these specific strata, but they suggest that other small deposits from before the rise of oxygen need to be carefully examined.

There are countless ways in which these chapters could be expanded and developed in future work. There are major manganese deposits from the Oligocene in the Baltic Sea area – for example, a reported deposit in Ukraine and Georgia with over a billion tons of manganese noted in Chapter 1 – which we were unable to acquire samples of. Since these are only approximately 30 million years old, it would be quite interesting to see what redox state(s) and minerals the manganese is in and determine to what extent it has post-depositional alteration. Similarly, this thesis has not explored the processes behind supergene manganese deposits. Somehow, oxic weathering has dissolved carbonate and surrounding material and produced a highly manganese-enriched deposit (like in the 1 billion-year-old Woodie-Woodie deposit in Australia or the 2 billion-year-old Postmasburg deposit in South Africa) but does that have microbial involvement? Recent work has shown that microbes can oxidize manganese from solids including manganese carbonates (e.g., Tang et al, 2013) and it would be interesting to do a microbial enrichment from some of these supergene deposits and explore the interactions between microbes and rocks in these deposits. Futhermore, the mineralogy of supergene deposits are necessarily different from other manganese deposits due to their formation, and preliminary work indicates they are Mn(III,IV) oxides with a large proportion of Mn(III) (see Appendix A). Pre-oxygen deposits could also be interrogated in more detail using methods established in this thesis: paired micro-scale X-ray spectroscopic imaging and X-ray absorption spectroscopy with optical microscopy and nano-scale electron microscopic analyses supplemented by Raman and X-ray diffraction methods. These in-depth analyses seem to be required for such ancient (and therefore necessarily corrupted by heat, pressure, and time) rocks which may or may not have primary manganese enrichments.

The Koegas Subgroup evidence for manganese-oxidizing photosynthesis also has several follow-up avenues. On the geological side, the manganese in this deposit is relatively unquantified and it would be illuminating to see how a better estimate of manganese volume compared with other post-oxygen manganese deposits. More investigations could be made into contemporaneous strata from Australia and Canada to see whether similar manganese-enriched sedimentary rocks could be found and compared to the Koegas Subgroup. Biological possibilities also abound: our lab has already begun to see whether we can produce a manganese-oxidizing cyanobacterium which cannot oxidize water and lives anaerobically, and that would be an exciting biological parallel to the geological data. And we are currently examining deep-branching cyanobacteria to see whether they might hold signs of manganese-oxidizing photosynthesis.

The calculations we made for quantifying oxygen from the presence and circumstances of oxygen-sensitive pyrite and uraninite grains were an improvement upon the existing models, which only used chemical weathering and did not incorporate physical erosion, but the chemical weathering equations also require refinement. The reaction rate for uraninite oxidation was developed in 1976 by Grandstaff, and there has been no published updates since this article. The commonly used pyrite oxidation law is also from one paper, now over ten years old, from Williamson and Rimstidt. Neither oxidation rate law explores the effects of microbial enhancement upon chemical weathering, which is highly unrealistic. With better chemical and biological constraints on pyrite and uraninite chemical weathering, our model for chemical dissolution and physical erosion could be much more accurate. Another improvement would be producing a model where physical erosion had a positive feedback on chemical weathering, as this is more similar to what occurs in natural environments.

The experiments we present measuring manganese phase through abiotic and biotic manganese reduction are just the beginning of an entire avenue of potential research. Ancient manganese deposits are often associated with iron deposits, like the Neoproterozoic Santa Cruz Formation in Brazil or the Koegas Subgroup in South Africa. Thus understanding the dynamics that occur with dual-oxide systems may be key to developing a realistic understanding of the processes that occurred in these formations. Experiments addressing this problem may involve biological reduction experiments with both iron oxides and manganese oxides, and varying levels of lactate to see if organic carbon abundance can control the amount of iron and manganese carbonate precipitation versus iron oxide products. Another exciting avenue to explore is the interactions that occur between sulfur and manganese, another combination commonly seen in nature (see Chapter 4). While we observed only manganese(II) cations produced from sulfide-induced manganese oxide reduction, others have noted manganese carbonate formation. This is likely due to the dissolved inorganic carbon controls and alkalinity influences on carbonate saturation. Future experiments to constrain when and how manganese carbonate may form in mixed manganese-sulfate/thiosulfate/sulfide systems might include *S. oneidensis* performing thiosulfate and sulfate reduction with Mn^{2+} present to measure whether manganese carbonate is formed, and sulfide-induced Mn(IV) reduction with a bicarbonate buffer and N_2/CO_2 gas mixture to see whether that stimulates manganese carbonate production (as I would predict) rather than the aqueous manganese(II) ions produced with PIPES buffer that we used. A third direction may be to test whether other electron donors like molecular hydrogen or fumarate affect mineralogy: this will help to constrain the requisite conditions for manganese carbonate and manganese(III) oxide formation. With manganese-enriched sedimentary rocks newly discovered on Mars, relating manganese minerals to environmental processes, and especially establishing whether any minerals are unique to biological processes, becomes even more important and stimulating.

The experiments suggested above have mainly addressed the astrobiological potential of understanding manganese mineralogy during various types of manganese reduction processes; however, another equally fascinating approach is exploring the mechanism of biological manganese reduction using the same flow-through real-time system we developed. One of the experiments we performed in Chapter 4, microbial manganese oxide reduction using *Shewanella oneidensis* under high phosphate, revealed that *S. oneidensis* effectively reduces manganese(IV) oxides in a two-electron process because Mn(II)-phosphate was immediately formed from Mn(IV) oxides. The mechanism of another common manganese-reducing microbe, *Geobacter sulfurreducens*, is thought to be different but is at present unclear. Using similar phosphate levels to ligate any Mn(II) produced, our flow-through system could be used to determine whether *G. sulfurreducens* also performs manganese reduction in a two-electron process or whether it has two one-electron steps. Pyrophosphate is a doubly-bound phosphate anion that is well-known for ligating to Mn(III) and pyoverdin is a siderophore with strong Mn(III) binding capacity. With both *S. oneidensis* and *G. sulfurreducens*, it would be interesting to add pyrophosphate and/or pyoverdin to the media rather than phosphate and see if a

Mn(III) phase is produced. It may be that there is Mn(III) produced by *S. oneidensis* but it is quickly reduced to Mn(II), and pyrophosphate or pyoverdin may be a way to halt the reaction at Mn(III). As discussed briefly in Chapter 4, there are two suggestions as to how *S. oneidensis* reduces solid oxides: either direct electron transfer by approaching the metal, which would suggest that the process has one-electron steps, or by using secreted soluble electron carriers called flavins. The exact mechanism that *S. oneidensis* uses could be tested with our flow-through real-time system by using a flavin mutant (developed in the Gralnick lab, U. Minnesota): does the mutant produce a Mn(III) intermediate before an Mn(II) shoulder appears? Performing this experiment in a phosphate-rich media might be especially illuminating, since with the non-mutant strain, no Mn(III) appears at all in phosphate-rich media. Additional experiments using pyrophosphate and/or pyoverdin may prove revealing as well if there are differences between the mutant and wild-type strains in the Mn(III) production and capture by these ligands.

There are a multitude of trajectories through which one can explore manganese cycling and manganese microbe-mineral-rock dynamics, and I wish every current and future adventurer the best of luck!

Appendix A

Supergene Manganese Preliminary Results

At the Kumba Iron Ore Mine, we sampled a small Mn deposit to understand the chemistry of the underlying sediments and the highly weathered supergene deposit, which may also be produced from hydrothermal fluid influences. These Mn deposits are known as ‘wad’ in mining jargon. We found that manganese was enriched over ten times more in the ‘wad’ deposit than the underlying carbonate (which was also quite weathered), and iron was enriched over fifteen times in the ‘wad’ material (Table A1). The manganese oxide in the ‘wad’ material was a mixture of MnIII and MnIV (Figure A1), which contrasts with our findings in Chapter 1 of modern manganese on the ocean.

TABLES AND FIGURES

Table A1: Comparing supergene deposit and underlying carbonate.

Analyte Symbol	MnO	SiO2	Al2O3	Fe2O3(T)	MgO	CaO	Na2O	K2O	TiO2	P2O5
Unit Symbol	%	%	%	%	%	%	%	%	%	%
Detection Limit	0.001	0.01	0.01	0.01	0.01	0.01	0.01	0.01	0.001	0.01
Analysis Method	FUS-ICP	FUS-ICP	FUS-ICP	FUS-ICP	FUS-ICP	FUS-ICP	FUS-ICP	FUS-ICP	FUS-ICP	FUS-ICP
KUMBA_WAD	8.686	18.22	9.1	40.8	5.16	1.98	0.07	0.08	0.371	0.51
KUMBA_CARB	0.818	0.35	0.17	2.51	18.89	29.82	0.02	0.01	0.004	0.01

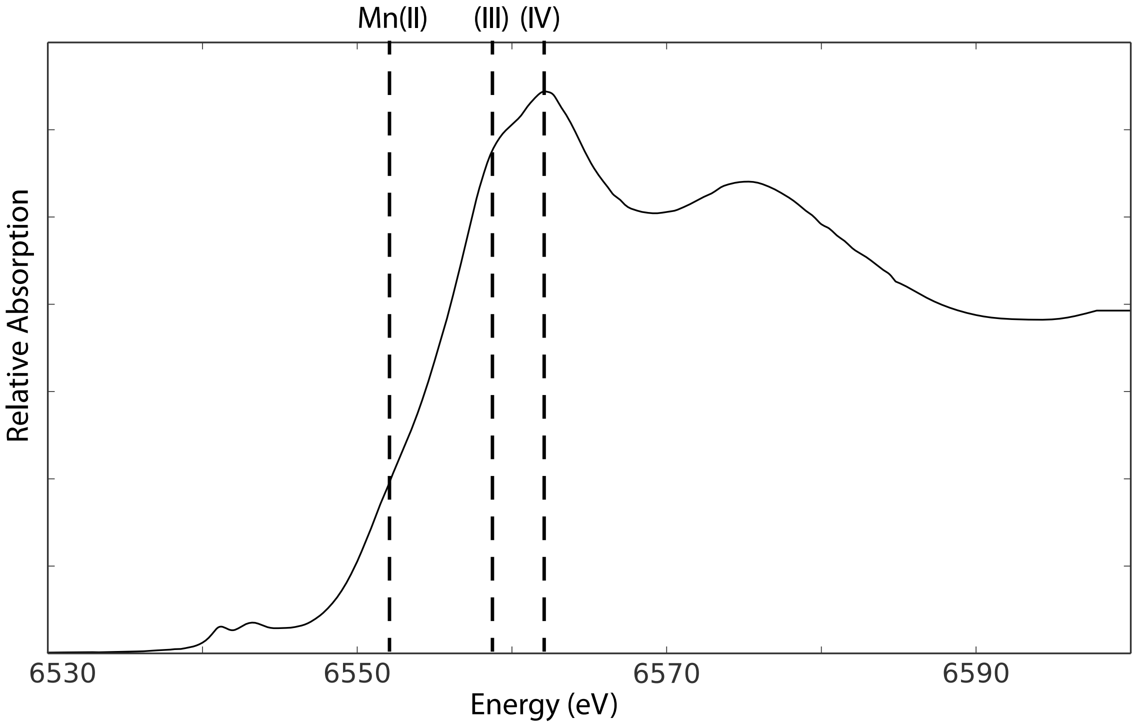

Figure A1: X-ray absorption spectra of Mn deposit.

Appendix B

Pongola-Witwatersrand examples of Mn enrichments

Manganese enrichments in Mozaan-Witwatersrand shales and iron formations have been used as evidence for environmental molecular oxygen (Smith et al., 2010; Planavsky et al., 2014). We used drill core sample chips provided to us by B. Smith (U Johannesburg) and prepared ultrathin (~15 μm) sections. We performed light and electron microscopy to document the textures and find regions where X-ray analysis would be the most valuable. We then obtained XAS spectra and images using two different synchrotron beam lines, beam line 10-2 and 2-3. Below are some of the salient details of each sample to accompany the figures.

Sample DDN-1 (Figure B1)

DDN-1 is a sandstone with abundant quartz grains, but it is also very rich in hematite and rhodochrosite, both as cements and veins. Hematite occurs as large well-crystalline needles largely as cements concentrated along laminae with larger grains sizes, and a very notable subhorizontal vein cross-cutting laminae. The carbonates are present also as cements and veins. There are small crystals of Mn-rich siderite as cement and thick veins composed of Mn-siderite, and/or Fe-rhodochrosite. There are also very large (> 100 μm) euhedral pyrites that cross cut the veins and other textures. Scattered Fe-aluminosilicates (that do not contain Mn) are present in cements. The XAS data show strong abundances of Mn confined largely to Mn-siderite and Fe-rhodochrosite in the cracks with lesser amounts in laminae with coarser sand. There are no high-valent Mn oxide phases present, only Mn(II). The high abundance of Mn in veins strongly implies a metasomatic origin in this sample. An image looking at the covariance of Mn and Fe shows that the Mn-Fe carbonate in the veins predates the hematite in the veins. The petrogenesis of this sample is complicated. The sample appears to have once been a quartz-dominated sandstone. Original cement is unclear but could have been clay minerals. Then fluids rich in Mn and Fe mineralized Mn-siderite and Fe-rhodochrosite in veins and cements in coarser laminae. This occurred either post- or syn-fracturing. The unusual and varied redox states of the vein mineralogy suggests several episodes of fluids. Oxidizing fluids mineralized hematite next. Then another generation of (more reducing and S bearing) fluids mineralized pyrites. Despite the complex petrogenesis of this sample, clear cross-cutting relationships help highlight instances of Mn and Fe mineralization tied to the migration of several generations of late fluids through the region.

Sample DBK-1 (Figure B2)

DBK-1 is a more complex sample with a much higher apparent metamorphic grade. The textures show a fine-grained matrix composed of magnetite, Fe/K clays, and quartz (cements) forming an incipient metamorphic foliation/lineation in a matrix around a large (cm-scale) nodule with a concentric chemical zonation defined by differing amounts of Fe and Mn, including very large euhedral pyrites (very clear in the Mn vs. Fe XAS plot). There is Ca- and Fe-rich, Al-poor spessartine throughout the sample, both in the nodule and in the dark iron-rich matrix. The garnets (low-Al spessartine and andradite) cross-cut all other grain boundaries. The most Mn-rich phases occur in the nodule as two coexisting very crystalline carbonate phases: a pseudo-kutnohorite ($Mn_{0.46}Ca_{0.41}Fe_{0.08}Mg_{0.04}CO_3$, labelled 'ku') and in an almost pure rhodochrosite ($Mn_{0.94}(Ca,Fe,Mg)_{0.06}CO_3$, labelled 'rh'). The carbonate phases are very coarsely crystalline and do not contain any inclusions of oxide phases. It is surprising that there is so little Fe in these carbonates: in Koegas Mn-enriched iron formations, the early diagenetic carbonate crystals are often highly enriched in iron as well as manganese and calcium (and a small amount of magnesium depending on dolomitization/ankeritization). And in the Hotazel, Fe is also present in trace domains of oxides throughout the kutnohorite and braunite. From grain boundaries here, it is difficult to constrain whether kutnohorite or rhodochrosite is earlier, with both appearing highly recrystallized. There is also a small amount of Mn in the Fe/K aluminosilicate minerals (1-2 wt. %), which is unusual. The SEM and X-ray absorption measurements produce independent and consistent mineralogy and redox state measurements, and no high valent Mn phases are present. The nodule here is a singularity: what appear to be additional small carbonate concretions throughout the sample under hand lens and light microscopy are highly-crystalline ellipsoid lenses of Fe/K aluminosilicates. Due to the high metamorphic grade, the petrogenesis is a bit tricky. The hypothesis that the nodule was composed of kutnohorite and precipitated during early diagenesis of Mn-oxide rich muds is attractive, but difficult to confirm with confidence. Because the primary lamination doesn't remain, it's not possible to assess differential compaction around the nodule. The lack of oxide inclusions and the coarse-grained nature of the carbonates could be the result of intense recrystallization of fine-grained pre-existing carbonates, and the garnets could result from decarboxylation of the carbonates at very high T, but can't be purely isochemical. The distinct chemical fronts associated with the growing front of the nodule are emphasized by the large trace metal-rich pyrites also give some pause. There are some potential metamorphic monazites present in there that could be used to date some of the alterations using the ion microprobe.

Sample PNG-3 (Figure B3)

Preliminary analyses indicate that PNG-3 is very similar to DBK-1. It too bears spessartine, rhodochrosite, and kutnohorite, but it additionally has another interesting Mn-bearing phase: a very Mn-rich chromite. Galena is also common. Rhodochrosite, which dominates the Mn composition of the sample, appears highly crystalline and does not contain any oxides. The spessartines are also much larger in diameter, around 20 microns rather than <10 microns in DBK-1. Garnets in this sample also have a surprising amount of Cr. At this metamorphic grade, it's difficult to interpret primary mineralogy, but would be great to examine material from the same horizon better preserved elsewhere.

FIGURES

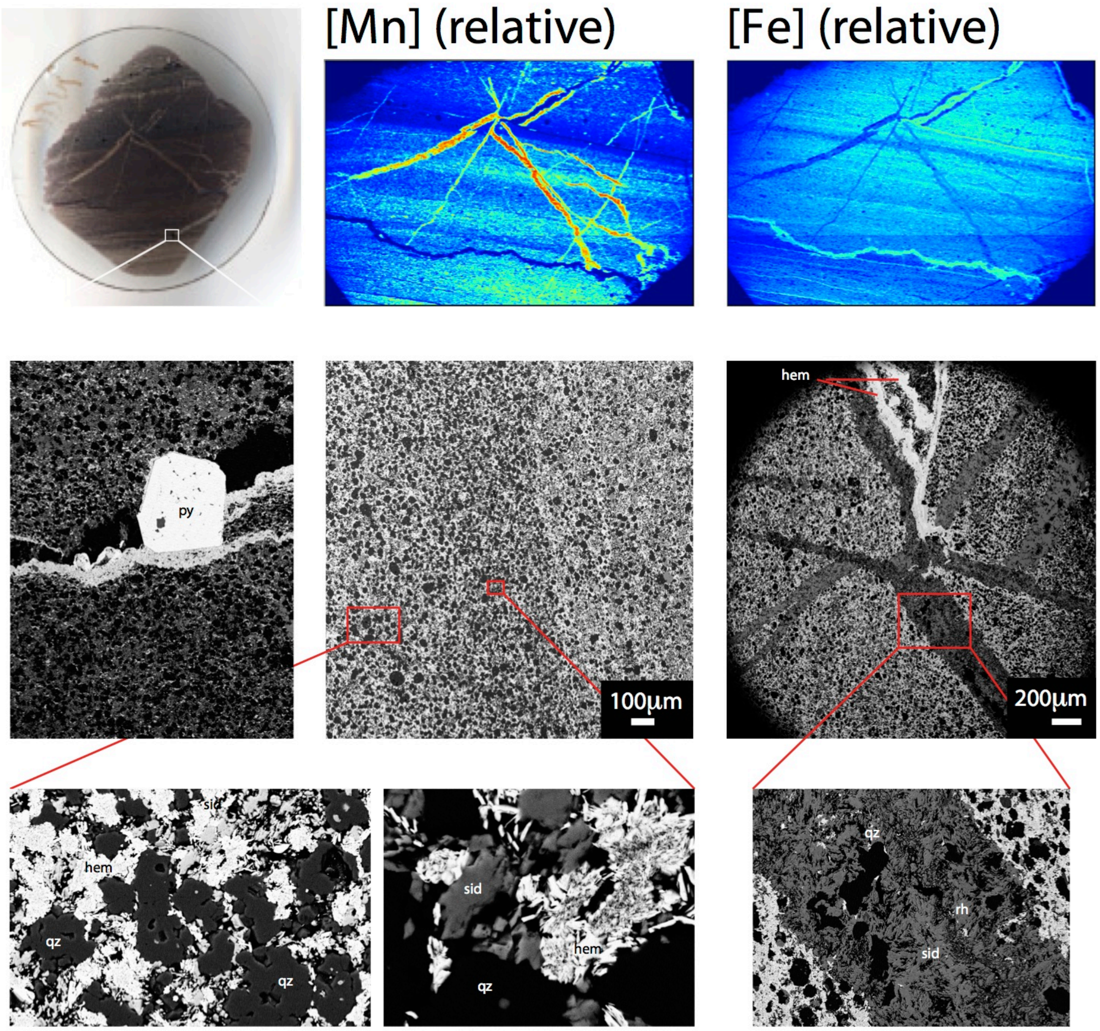

hem = hematite, sid = $Fe_{0.5\text{-}0.6}Mn_{0.4\text{-}0.5}CO_3$, rh = $Mn_{0.68}Fe_{0.31}Ca_{0.02}CO_3$,

py = pyrite qz = quartz

Figure B1: Mn- and Fe- enriched sandstone from DDN-1 core with large cross-cutting veins. See above for further details.

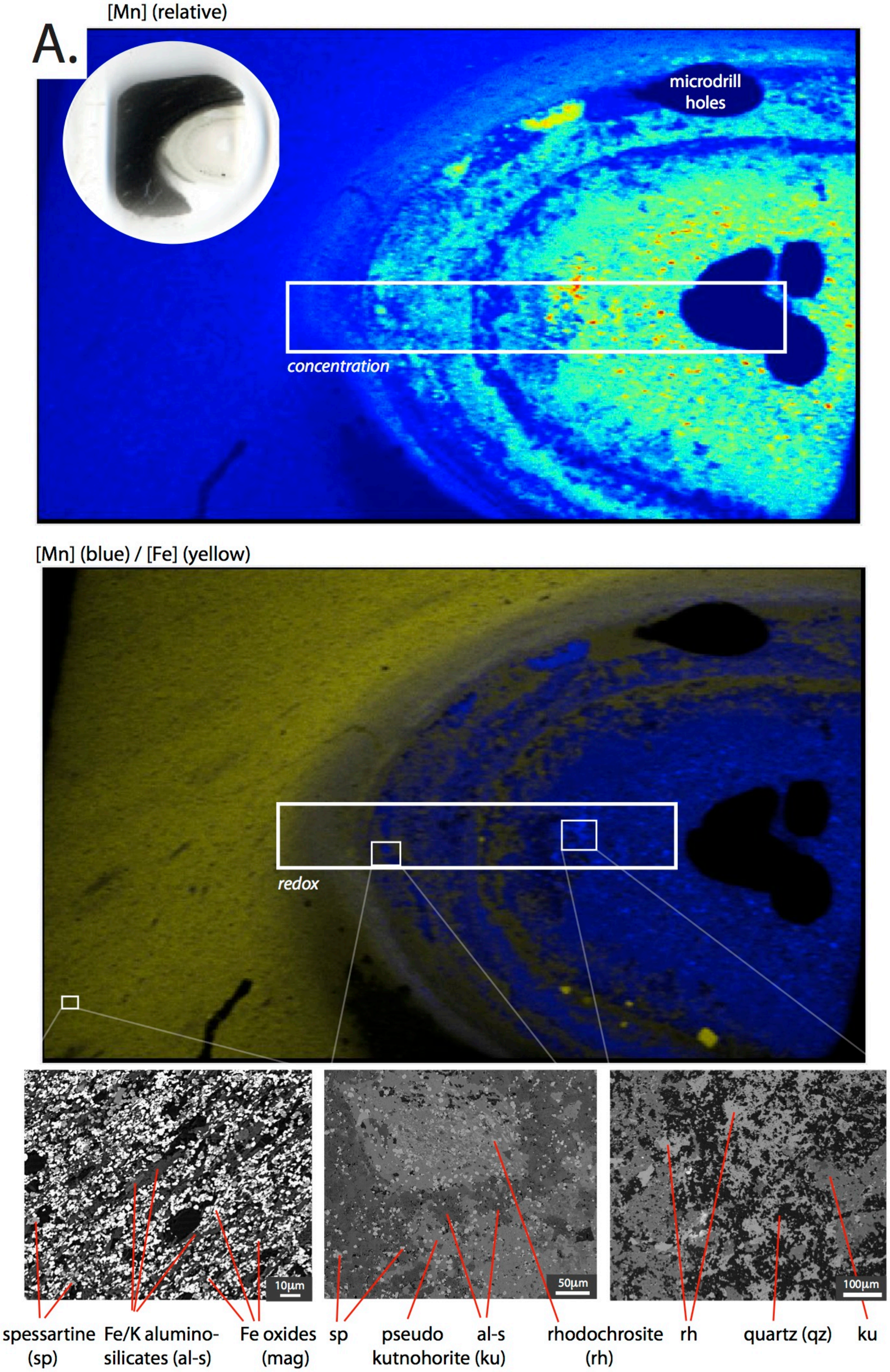
A.
[Mn] (relative)
microdrill holes
concentration
[Mn] (blue) / [Fe] (yellow)
redox
10µm
50µm
100µm
spessartine (sp)
Fe/K alumino-silicates (al-s)
Fe oxides (mag)
sp
pseudo kutnohorite (ku)
al-s
rhodochrosite (rh)
rh
quartz (qz)
ku

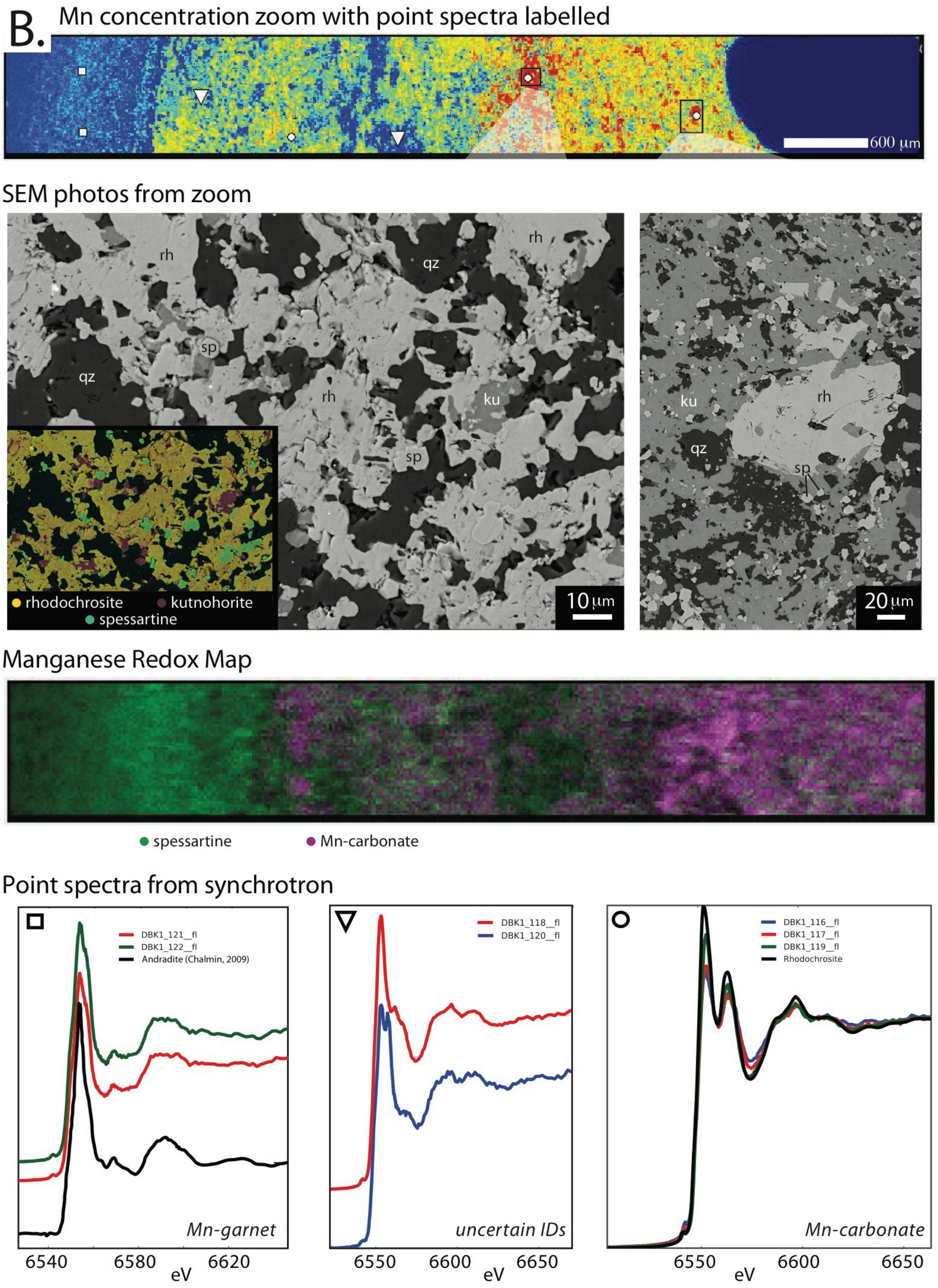
B.
Mn concentration zoom with point spectra labelled
600 μm
SEM photos from zoom
rh
qz
rh
sp
qz
rh
ku
sp
rhodochrosite
kutnohorite
spessartine
10 μm
ku
rh
qz
sp
20 μm
Manganese Redox Map
spessartine
Mn-carbonate
Point spectra from synchrotron
DBK1_121__fl
DBK1_122__fl
Andradite (Chalmin, 2009)
Mn-garnet
6540
6580
6620
eV
DBK1_118__fl
DBK1_120__fl
uncertain IDs
6550
6600
6650
eV
DBK1_116__fl
DBK1_117__fl
DBK1_119__fl
Rhodochrosite
Mn-carbonate
6550
6600
6650
eV

Figure B2 (above): Manganese-enriched concretion from DBK-1 core. A. Large-scale observations using synchrotron X-ray fluorescence and spectroscopic mapping and SEM-EDS identifications. B. Microscale analyses using synchrotron X-ray spectroscopic mapping and SEM-EDS identifications.

Figure B3 (below): Manganese analyses on PNG-3 core sample, showing Mn-enriched garnet (spessartine), rhodochrosite, kutnohorite, and Mn-rich chromite.

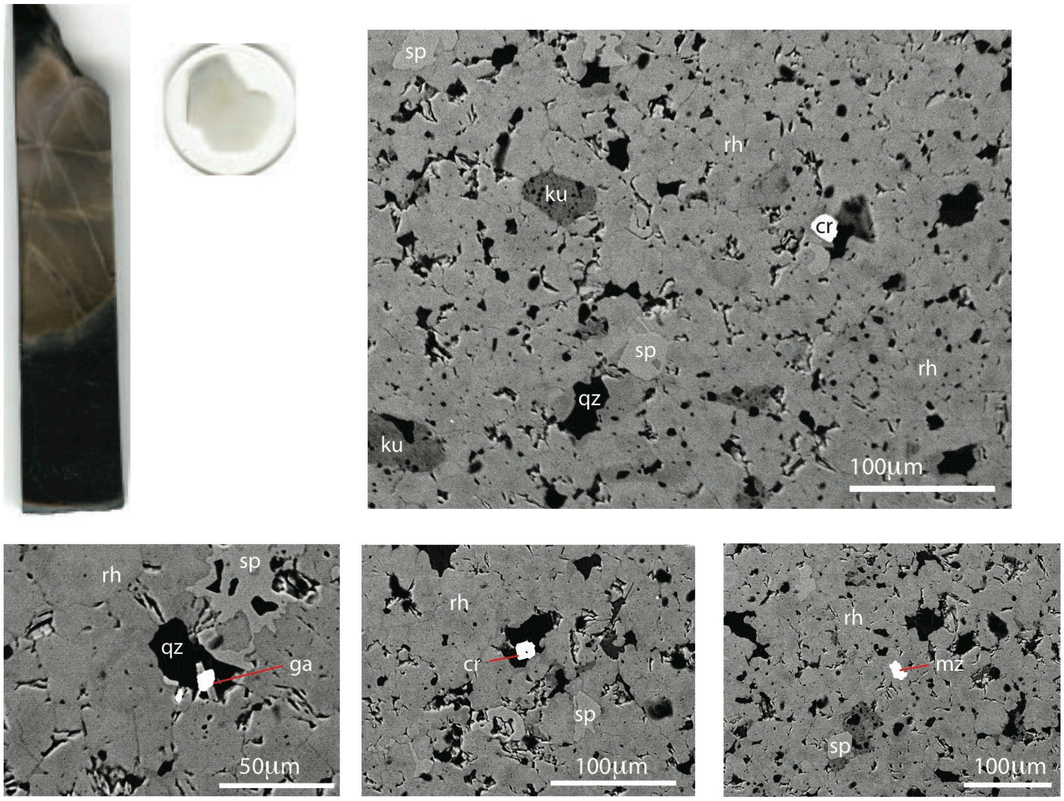

sp = Ca-enriched spessartine (Mn-garnet), rh (here)= $Mn_{0.96}Ca_{0.03}CO_3$, ga = galena

ku (here) = $Mn_{0.67}Ca_{0.39}Fe_{0.04}Mg_{0.02}CO_3$, qz = quartz mz = monazite cr = chromite-like min

Cr-enriched bright mineral with Mn: EDS Spectra

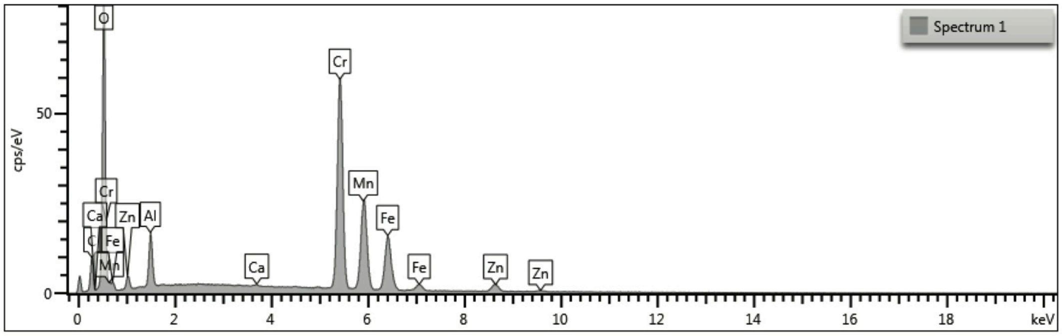

REFERENCES CITED

Planavsky N. J., Asael D., Hofmann A., Reinhard C. T., Lalonde S. V., Knudsen A., Wang X., Ossa Ossa F., Pecoits E., Smith A. J. B., Beukes N. J., Bekker A., Johnson T. M., Konhauser K. O., Lyons T. W. and Rouxel O. J. (2014) Evidence for oxygenic photosynthesis half a billion years before the Great Oxidation Event. *Nat. Geosci.* **7**, 283–286.

Smith A. J. B., Beukes N. J., Gutzmer J. and Cochrane J. M. (2010) Evidence for dissimilatory manganese reduction and availability of free molecular oxygen during deposition of Mesoarchean Witwatersrand-Mozaan strata. *Mineral. Mag.* **74**, A973.

Appendix C

Changing redox states in iron formations across the GOE

We have examined the redox state(s) in a number of samples from iron formations before and after the Great Oxidation Event (GOE) using synchrotron X-ray absorption spectroscopy. These analyses included both X-ray fluorescence of iron and X-ray spectroscopic mapping, and, when possible, supplementary X-ray absorption spectra. Our results were consistent with previous observations made by Klein and indicate that a major change occurred in how iron was stabilized (and possibly originally deposited) before and after the GOE and in Neoproterozoic iron formations (Klein, 2005).

The ca. 3.2 Ga Moodies Group earlier in the Archean has both oxidized and reduced iron, probably in hematite and iron carbonate phases, but there are mainly reduced iron phases like Fe(II,III) silicates, magnetite, carbonate, and pyrite in the late Archean to early Paleoproterozoic Kuruman Formation, Mt. Sylvia Formation and Koegas Subgroup (Figure C2,C3,C4). If this is a real iron redox transition, it is interesting to speculate whether this change may relate to the advent of iron-reducing metabolisms or increase in organic carbon and productivity. After the GOE, iron oxides return again (Figure C5, C6) – suggesting that with oxygen present, iron was no longer completely reduced in the sediments. Later in the glaciation-associated iron formations of the Neoproterozoic, the iron mineralogy changed completely to all hematite (Figure C7, C8). The lack of reduced iron minerals including iron carbonate demonstrates that the iron and carbon cycles were not linked at this time (suggesting little organic carbon was reaching the sedimentary floor) and that iron-reducing metabolisms were not reducing these iron oxides.

FIGURES

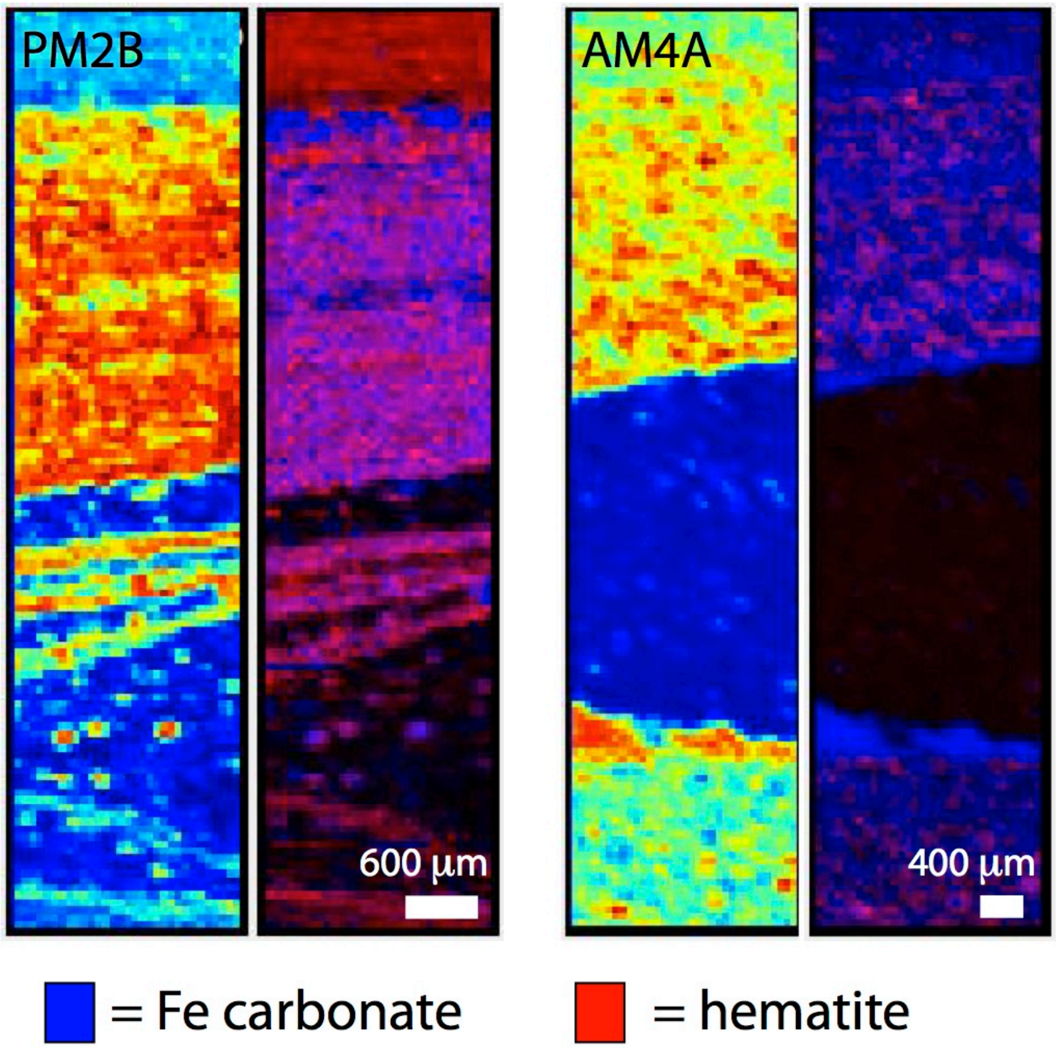

Figure C1 – Representative samples from the ca. 3.2 Ga Moodies Group, S Africa, showing best-fitting to Fe-carbonate and hematite.

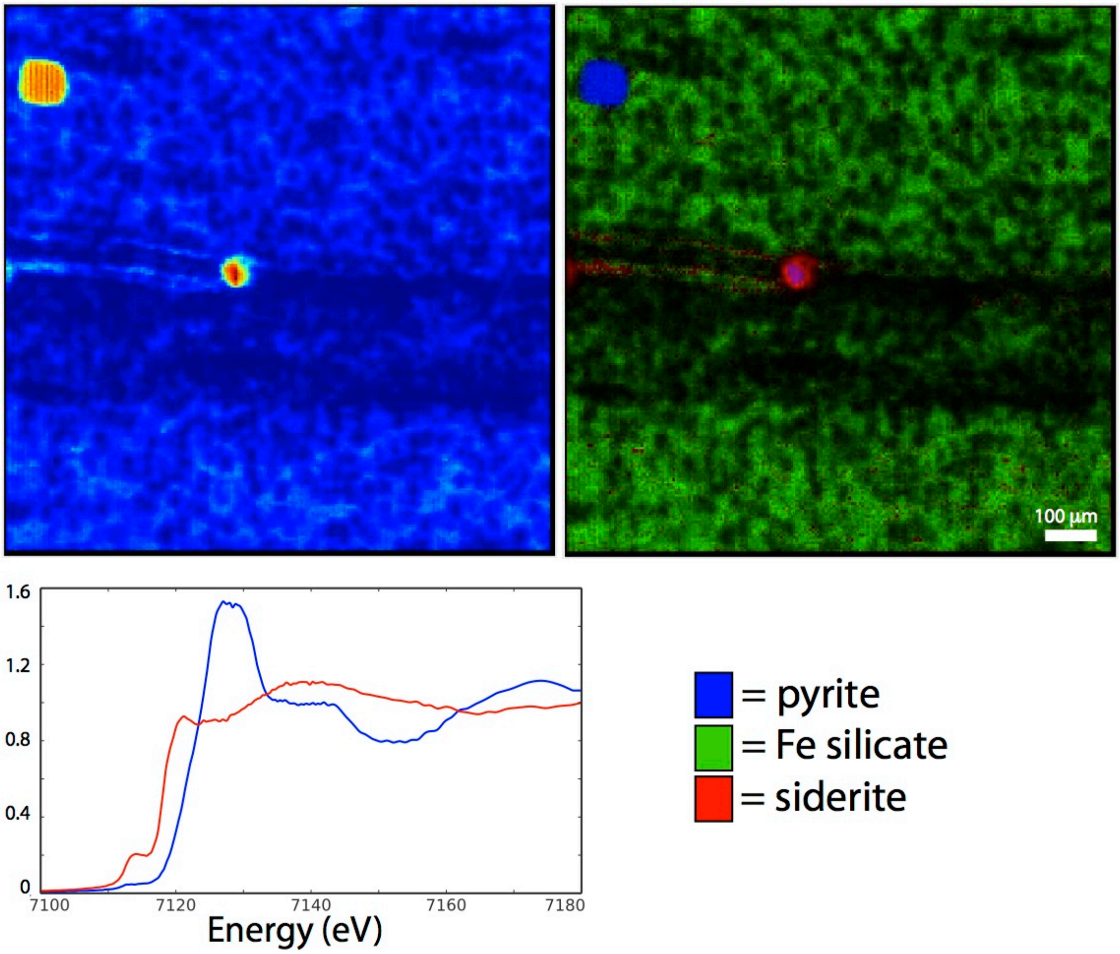

Figure C2 – Representative sample from the ca. 2.5 Ga Kuruman Formation, S Africa, showing abundant iron silicates and less common pyrite and siderite particles. Iron silicate spectra shown in blue and pyrite spectra shown in red. Speciation maps have iron silicates shown in green, siderite in red, and pyrite in blue.

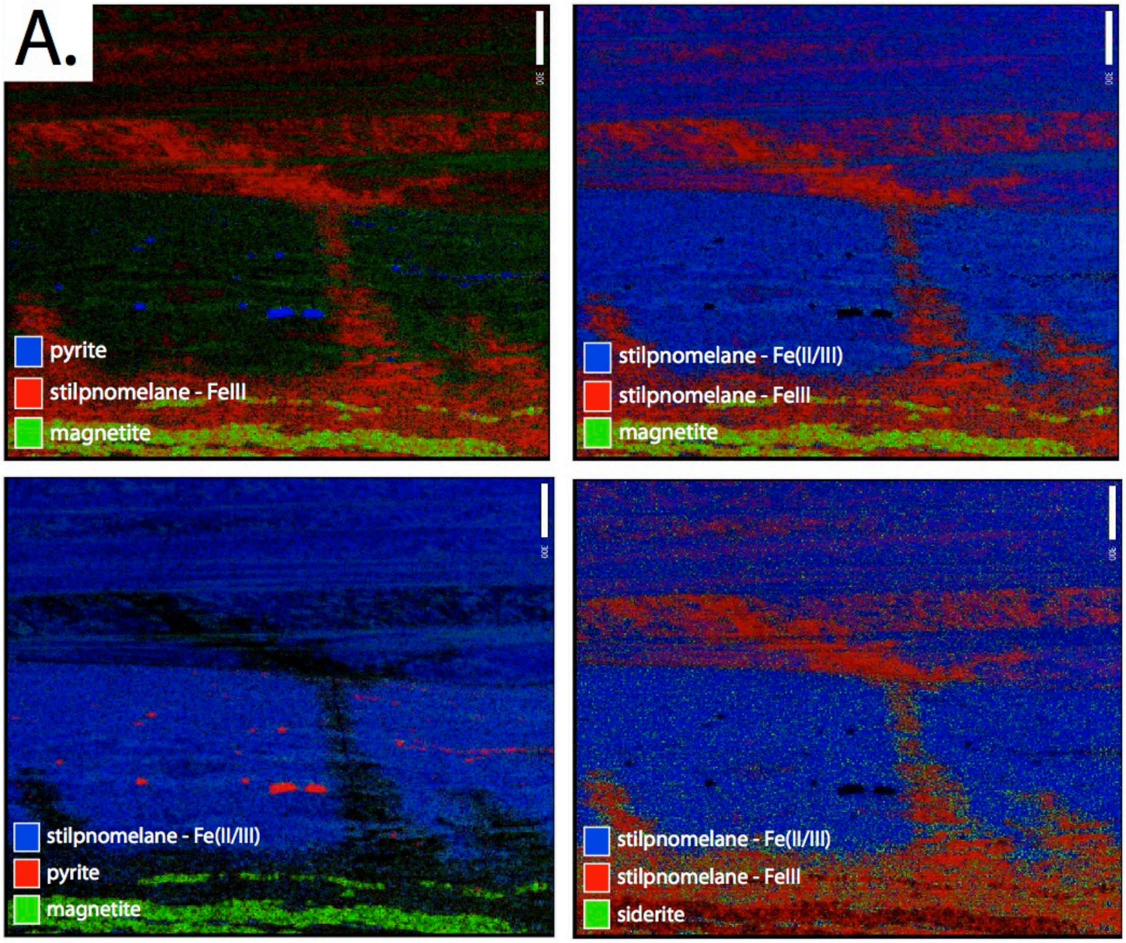
A.
300
pyrite
stilpnomelane - FeIII
magnetite
stilpnomelane - Fe(II/III)
stilpnomelane - FeIII
magnetite
stilpnomelane - Fe(II/III)
pyrite
magnetite
stilpnomelane - Fe(II/III)
stilpnomelane - FeIII
siderite

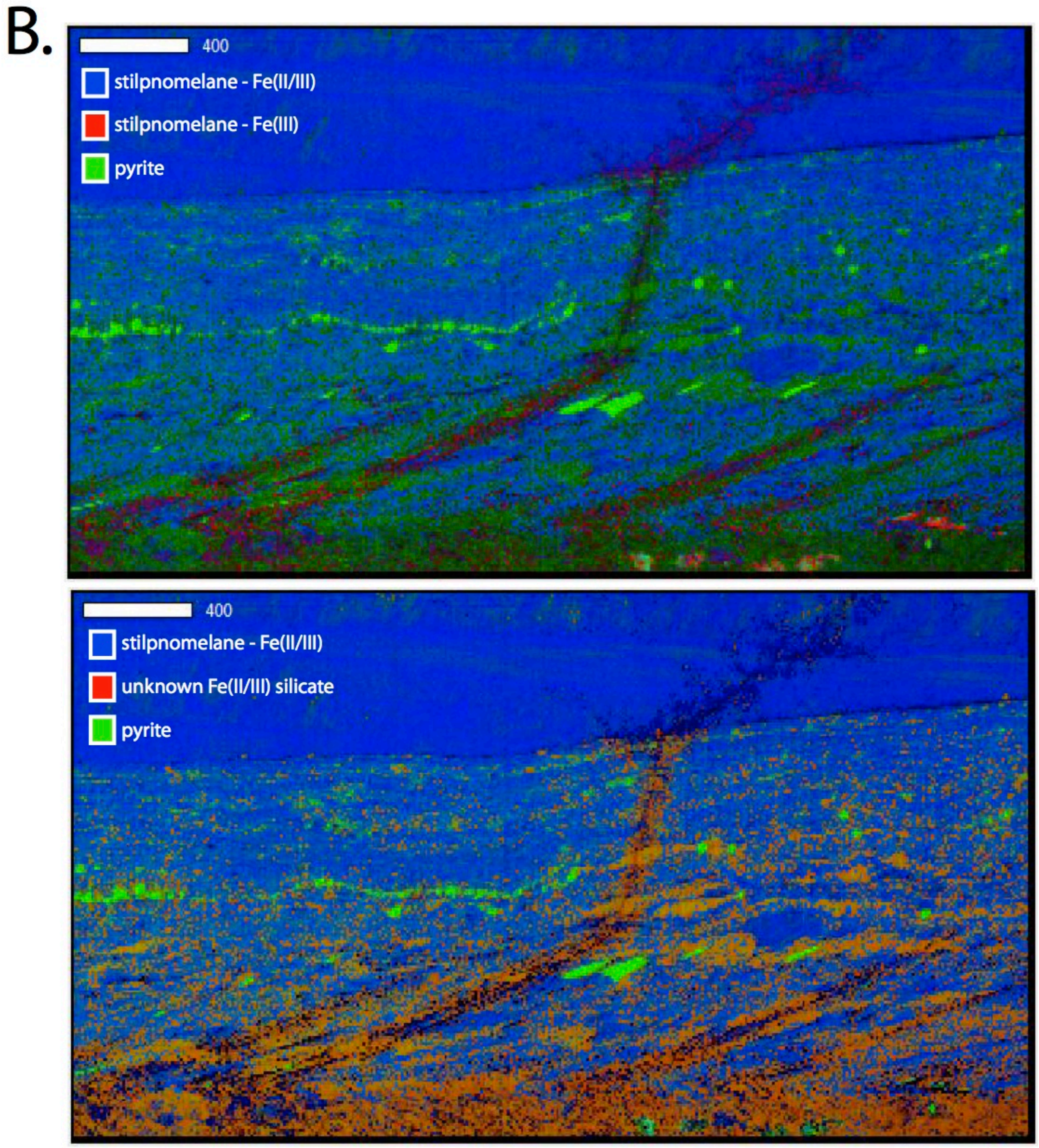

Figure C3 – Representative regions from the ca. 2.5 Ga Mt. Sylvia Formation, Australia, showing many iron silicates, seams and crystalline pyrite, and bands of magnetite.

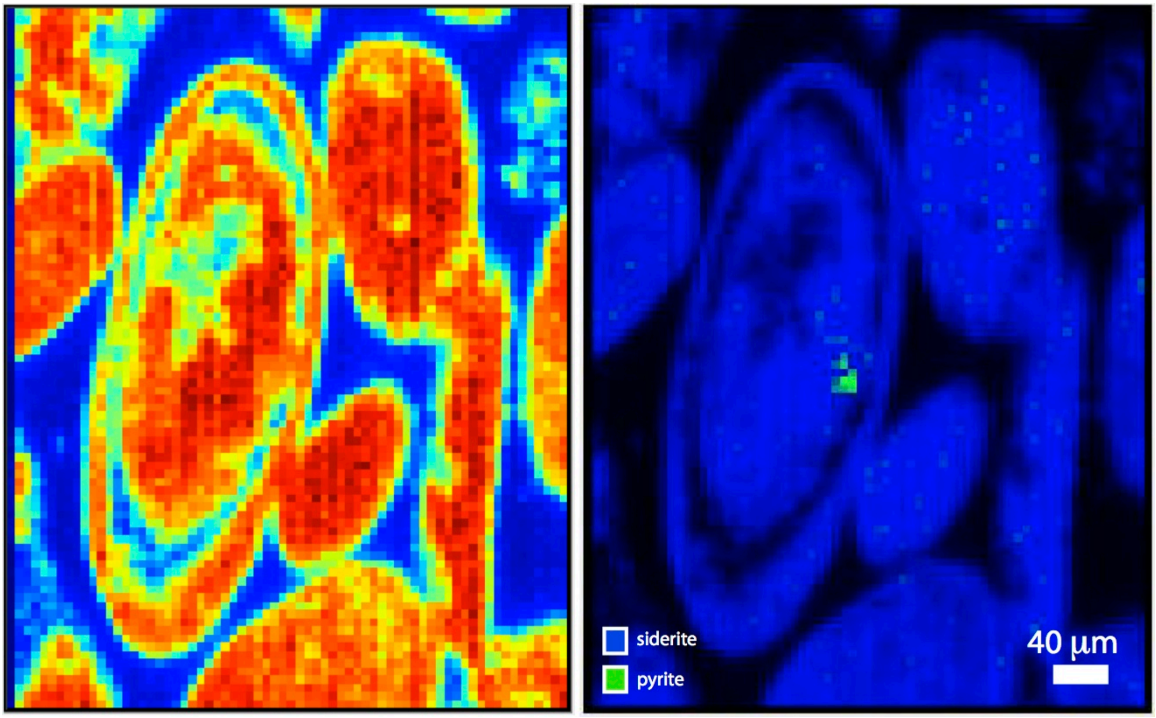

Figure C4 – Representative area from the ca. 2.4 Ga Koegas Subgroup, S Africa, showing Fe-carbonate ooids and siderite.

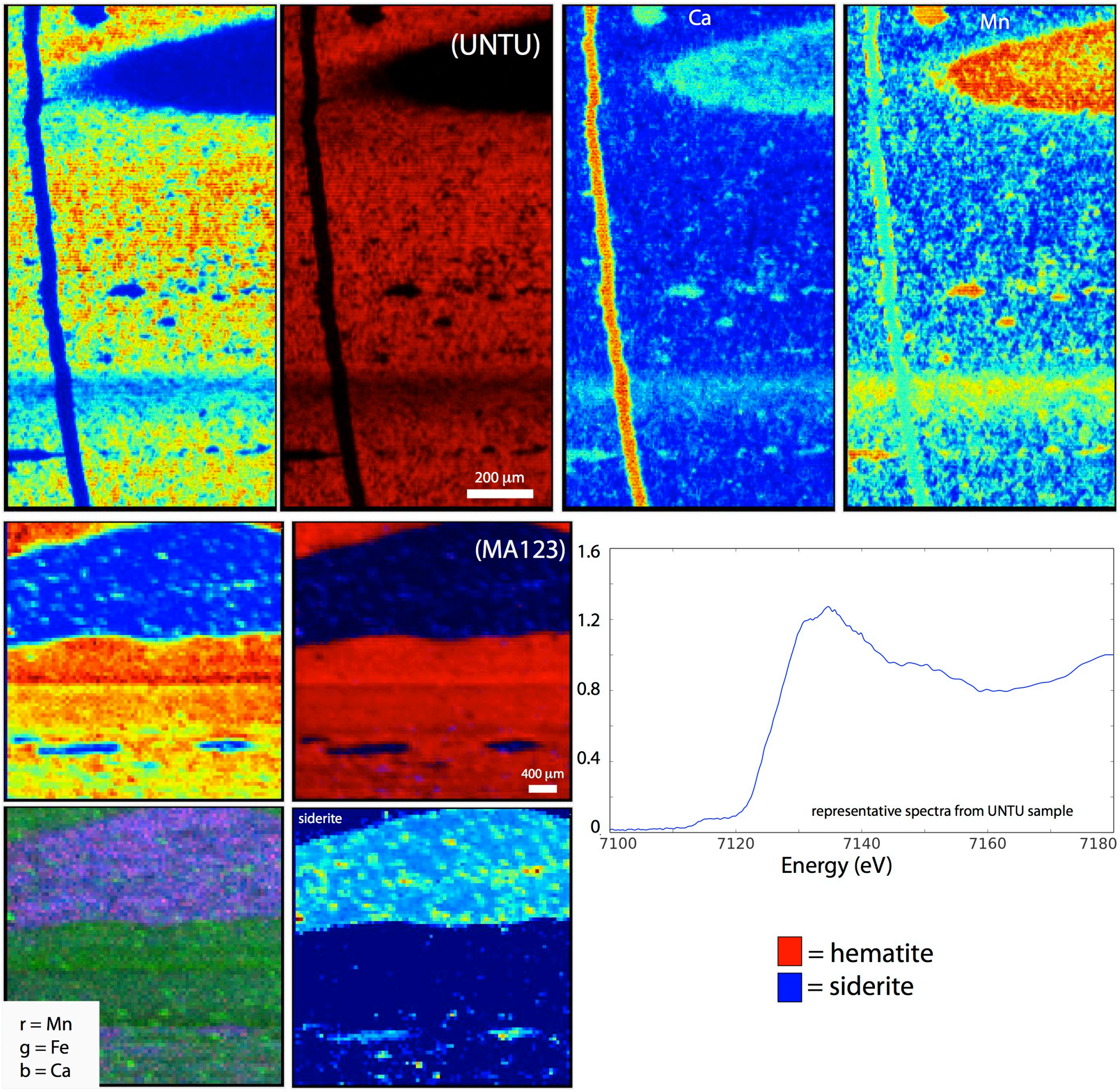

Figure C5 – Representative samples from the ca. 2.2 Ga Hotazel Formation, S Africa, showing hematite with chert and siderite nodules.

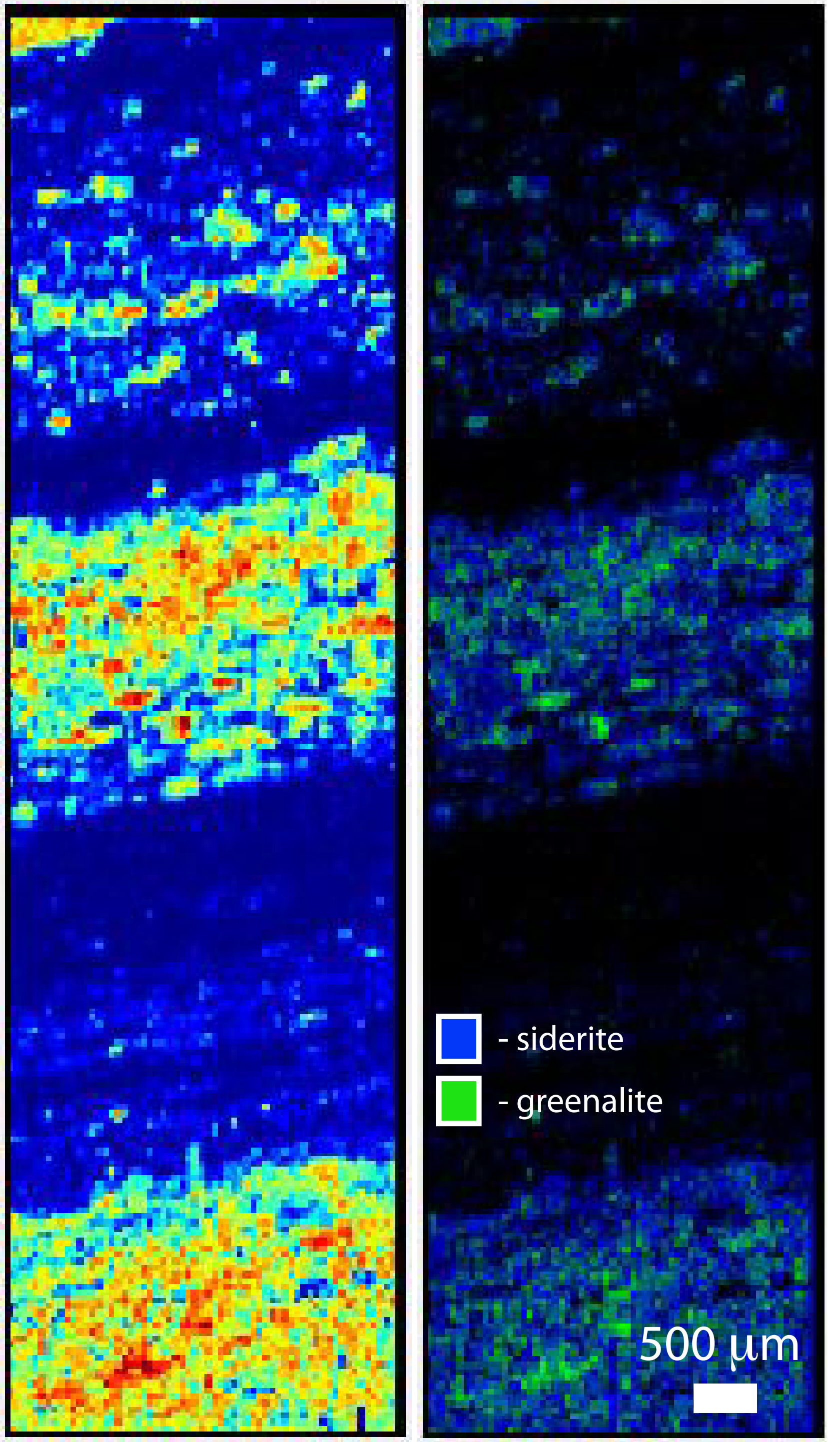

Figure C6 – Representative sample from the ca. 1.8 Ga Gunflint Formation, Canada, best fitting iron carbonate and greenalite. Others have observed additional minerals at this time, including hematite, magnetite, berthierine, and glauconite (Wilson et al., 2010).

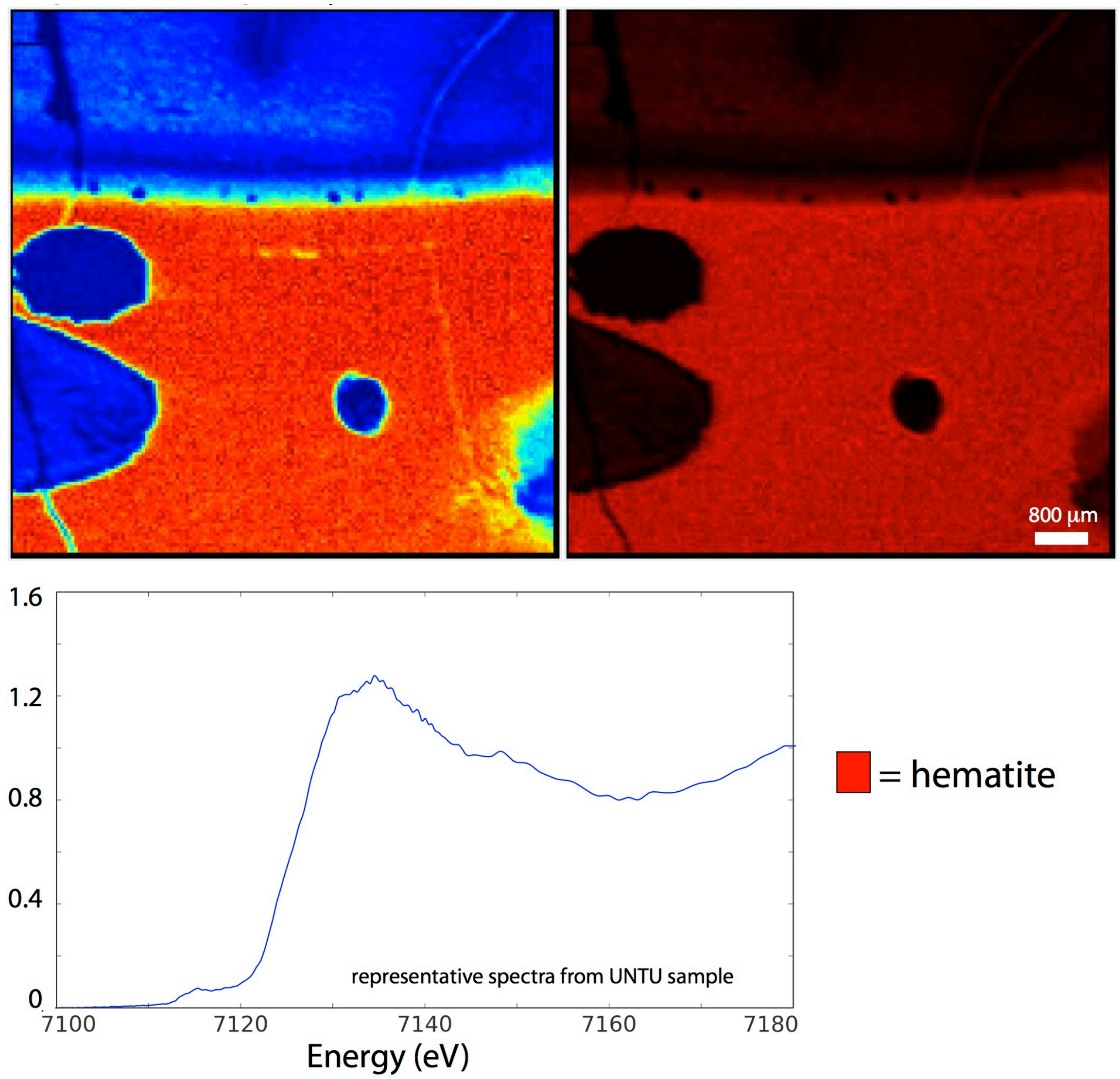

Figure C7 – Representative sample from the ca. 730 Ma Rapitan Group, Canada, showing only hematite.

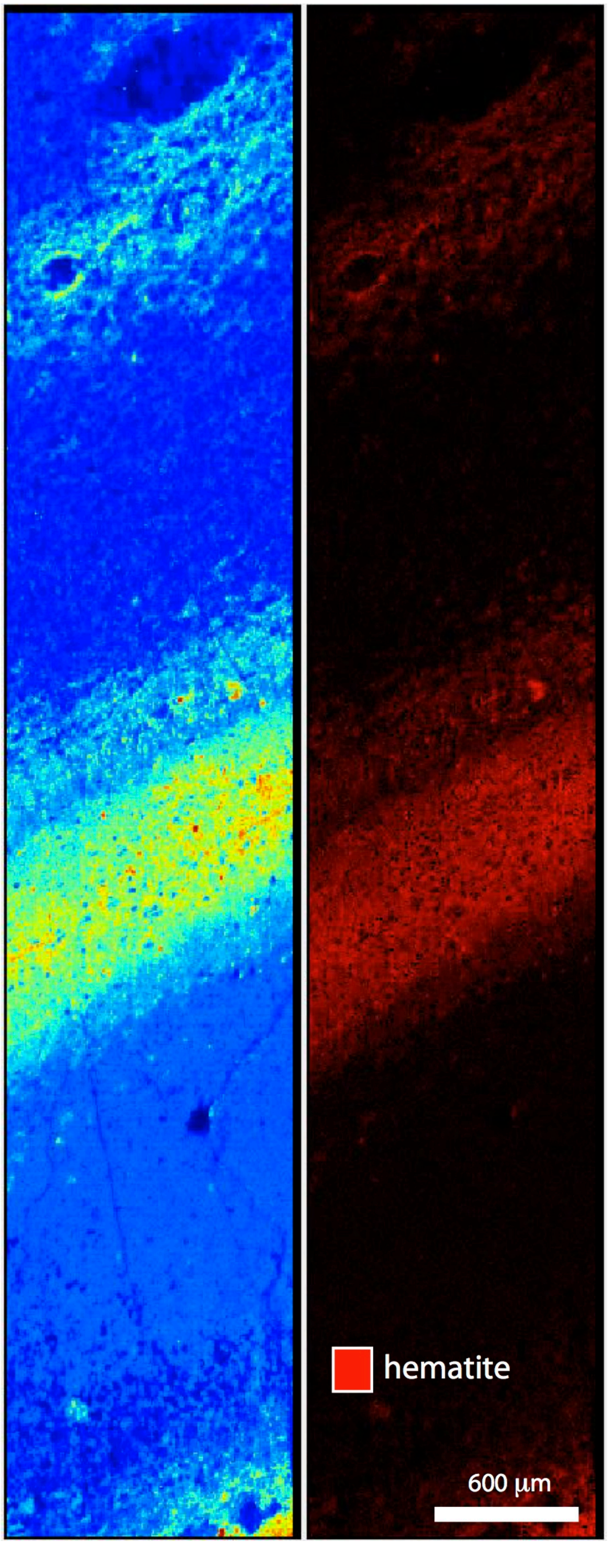

Figure C8 – Representative sample from the ca. 630 Ma Santa Cruz Formation, Brazil, showing best-fitting to hematite.

REFERENCES

Klein C. (2005) Some Precambrian Banded Iron-Formations (BIFs) from Around the World: Their Age, Geologic Setting, Mineralogy, Metamorphism, Geochemistry, and Origins. *Am. Mineral.* **90**, 1473–1499.

Wilson J. P., Fischer W. W., Johnston D. T., Knoll A. H., Grotzinger J. P., Walter M. R., McNaughton N. J., Simon M., Abelson J., Schrag D. P., Summons R., Allwood A., Andres M., Gammon C., Garvin J., Rashby S., Schweizer M. and Watters W. A. (2010) Geobiology of the Late Paleoproterozoic Duck Creek Formation, Western Australia. *Precambrian Res.* **179**, 135–149.